Mécanique & Industries 11, 309–326 (2010)
DOI: 10.1051/meca/2010045

www.mecanique-industries.org

Mécanique & Industries

Identification of constitutive properties of a laminated rotor at rest through a condensed modal functional

Guillaume Mogenier[1,a], Nouri-Baranger Thouraya[1], Regis Dufour[1], Lionel Durantay[2] and Nicolas Barras[2]

[1] Université de Lyon, CNRS, INSA-Lyon, LaMCoS UMR 5259, 18–20 rue des sciences, 69621 Villeurbanne, France
[2] Converteam SAS, Rotating Machines Division, 442 rue de la rompure, 54250 Champigneulles, France

Received 12 May 2009, Accepted 7 June 2010

Abstract – Predicting the dynamic behavior of laminated rotors in bending requires the identification of the bending rigidity of the laminated core. An identification of constitutive properties is proposed on the rotor at rest, which is a first step for rotordynamics prediction. Modal parameters predicted and measured are included in a functional based on a hybrid Rayleigh quotient and combined with the Guyan method, the master degrees of freedom corresponding to the measurement points. The laminated core rigidity is extracted through a Levenberg-Marquardt minimization.

Key words: Vibration / identification / optimization / Rayleigh quotient / laminated rotor / squirrel cage

Résumé – Identification des propriétés constitutives d'un rotor à cage d'écureuil à l'arrêt par une fonctionnelle modale condensée. Pour prévoir le comportement dynamique en flexion des rotors à cage d'écureuil, une procédure d'optimisation est proposée pour identifier la rigidité en flexion de la partie feuilletée. Les quantités modales calculées et mesurées sur un rotor feuilleté sont incluses dans une fonctionnelle basée sur un quotient de Rayleigh hybride et combinée à la méthode de condensation de Guyan. Les degrés de liberté de contour sont alors associés aux points de mesure. Une minimisation de Levenberg-Marquardt permet d'extraire la rigidité de la partie feuilletée.

Mots clés : Vibration / identification / optimisation / quotient de Rayleigh / rotor feuilleté / cage d'écureuil

1 Introduction

This article deals with high speed induction motors HSM used in critical applications such as in the gas industry. They operate within a range from 6000 to 18 000 rpm and supply a power from 3 to 30 MW. Squirrel cage rotors are composed of two forged steel shaft-ends and a core of laminated steel held by prestressed tie rods located at the periphery of the magnetic mass and embedded at the end of each shaft (see Fig. 1). The squirrel cage is composed of short circuit rods also positioned at the periphery of the magnetic mass and connected to two short circuit rings located at the ends of the laminated core. The tie rods therefore exert prestress compression on the ring-laminated core assembly that makes modeling difficult.

Models of this type of rotor in the literature are rare [1–4]. Articles devoted to rotors composed of a stack of laminations shrunk onto a central shaft are more common. In [5], the authors evaluate the influence of the length of the core on the natural frequencies of a three dimensional finite element model of a permanent brushless machine. In [6], a branched model is obtained by modeling the magnetic mass by an assembly of rings linked together and to a central shaft elastically. In [7], the magnetic mass

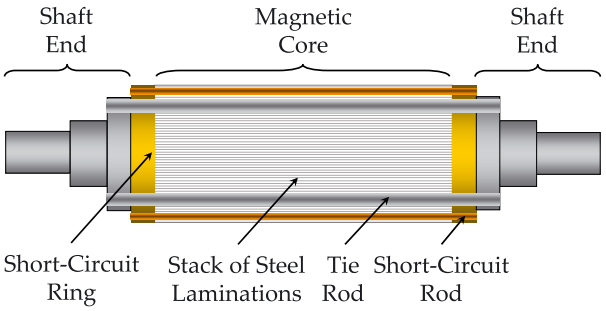

Fig. 1. Scheme of a HSM rotor.

[a] Corresponding author: guillaume.mogenier@insa-lyon.fr

Nomenclature

Roman letters	
a	Ratio of inner and outer diameters
c	Coordinate of the projection of the partial derivative of an eigen-vector in the modal basis
C	Non symmetric matrix including gyroscopic and damping effects
d	Diameter (m)
E	Young's modulus ($\mathrm{N{\cdot}m^{-2}}$)
$\mathscr{E}$	Error estimate based on predicted and measured mode shapes
f	Global functional
F	Global vector containing forces (N)
$\mathscr{F}$	Error estimate based on predicted and measured natural frequencies and mode shapes
g	Standard gravity acceleration ($\mathrm{m{\cdot}s^{-2}}$)
G	Shear modulus ($\mathrm{N{\cdot}m^{-2}}$)
H	Approximated Hessian matrix of the global functional f
I	Identity matrix
I_{G_y}	Second moment of inertia of the cross section ($\mathrm{m^4}$)
J	Jacobian matrix of the error estimate $\mathscr{E}$
k	Shear coefficient of the cross section
k_e	Lateral stiffness at the free end of the rotor
k_l	Lateral stiffness of the flexible sling
$\mathscr{K}$	Element of the domain Ω
K	Stiffness matrix
l	Length (m)
L_e	Length of a flexible sling (m)
L_r	Length of the rotor (m)
m	Number of eigen-elements
m_r	Mass of the rotor (kg)
M	Mass matrix
n	Number of optimization variables
n_c	Number of master degrees of freedom
n_δ	Total number of degrees of freedom
n_i	Number of slave degrees of freedom
N_e	Total number of finite-elements
N_ti	Total number of tie rods
$\mathscr{R}$	Rayleigh quotient ($\mathrm{rad^2.s^{-2}}$)
$\mathscr{R}^*$	Hybrid Rayleigh quotient ($\mathrm{rad^2.s^{-2}}$)
S	Cross section ($\mathrm{m^2}$)
t	Time (s)
v	Lateral deflection (m)
x	Vector containing n optimization variables
x^*	Vector containing the optimal values of the optimization variables
$\hat{x}$	Vector containing n optimization variables in the neighborhood of the optimum x^*
Y	Arbitrary vector
z_G	Axial position of the center of mass of the rotor (m)
Greek lettres	
α	Lower boundary of an interval containing an optimization variable
β	Upper boundary of an interval containing an optimization variable
γ	Descent direction of the optimization algorithm
δ	Degrees of freedom of the complete finite-element model
Δ	Variation
ε	Scalar much lower than unity
θ	Rotation of the cross section (rad)
λ	Bending eigen-value ($\mathrm{rad^2.s^{-2}}$)
μ	Damping (or Marquardt) parameter
ρ	Density ($\mathrm{kg.m^{-3}}$)
υ	Poisson ratio

Nomenclature. continued.

σ	Bijection
Σ	Set containing the degrees of freedom
τ	Descent step of the optimization algorithm
φ	Bending mode shape
ϕ_y	Shear factor
χ	Bijection parameter
ψ	Guyan transformation matrix
ω	Bending natural frequency (rad.s^{-1})
∇	Differential operator
Subscripts	
Ω	Domain containing the finite-elements of the model
c	Master degrees of freedom
ext	Exterior
f	Elastic stiffness
i	Slave degrees of freedom
int	Inner
k	kth mode
N	Longitudinal axis
p	pth optimization variable
G	Geometric stiffness
$0p$	Reference value
q	qth optimization variable
θ	Rotation effects
v	Translation effects
ti	Tie rods
u	Objects dependent on optimization variables x
Upperscripts	
$^e()$	Relative to the eth element $\mathscr{K}$
c	Relative to the master degrees of freedom
i	ith iteration of the optimization algorithm
r	Relative
$\tilde{()}$	Relative to the condensed finite-element model
$\hat{()}$	Relative to experimental data
$\dot{()}$	Time derivative
Abbreviations	
HSM	High Speed Motor
MAC	Modal assurance criterion
NCO	Normalized cross orthogonality
d.o.f.	Degree of freedom

is modeled by branched beams and an equivalent Young's modulus whereas [6] uses an orthotropic material whose behavior law depends on the properties of the laminated sheet and the flexibilities of the interfaces generally composed of a layer of resin or varnish that significantly reduces the equivalent Young's modulus of the core [8]. A coefficient known as stacking factor is then considered to adjust the specific gravity of the core [9,10]. In [11], the authors show that the natural frequencies of a laminated rotor increase significantly with the prestress compression of the laminated core and they model the magnetic mass by using an equivalent diameter and lumped masses. Consequently, the rigidity of the laminated magnetic mass is difficult to model and it is usually necessary to perform an identification procedure with modal analyses.

In modal identification methods, functionals are defined to quantify the difference between predicted and measured natural frequencies [12] and mode shapes [13]. It is therefore necessary to use an optimization method to minimize this difference by updating the parameters to be identified for use in a numerical model so that the model's quantities of interest tend towards target values, i.e. the experimental data. A multicriteria functional based in particular on natural frequencies and the terms of the modal assurance criterion matrix MAC is proposed in [14]. In [15], the authors minimize a functional using the sensitivity matrix of a model in order to identify the elastic properties of a laminated material. The disadvantage of these methods is that they use weighting coefficients for each component of the functional. The Levenberg-Marquardt algorithm, which is used to minimize this functional, requires prior knowledge of the derivatives of the eigen-values [16] and eigen-vectors that can be obtained by approximate modal methods [17] or exact methods [18].

This article presents a finite-element model of the rotor comprising a squirrel cage. An identification procedure based on an energy functional [19], is embedded with the Guyan reduction method [20] so that the dimensions of the numerical and experimental mode shapes are the same. Accordingly, between each mode, homogenous terms are obtained that result from the combination of a natural frequency and its associated mode shape that do not require weighting coefficients. The choice of performing condensation rather than expansion is driven by the desire to conserve only the initial experimental data and not their approximations synthesized in the form of nodes for which no experimental information exists, as in the case of the SEREP (System Equivalent Reduction Expansion Process) and Guyan expansion methods [21,22]. This procedure permits identifying the constitutive properties of the laminated core by minimizing the difference between the modal quantities calculated with the finite-element beam model containing few degrees of freedom (d.o.f.), and measured during a non rotating modal analysis under free-free conditions. Although a beam model is used, shear modulus is defined as being independent of the Young's modulus and the Poisson ratio in order to account for the orthotropic nature of the laminated core [6]. This research constitutes the first step of a global strategy aimed at predicting the dynamic behavior in bending of squirrel cage rotors in order to achieve more complex modeling that takes into account, for example, a modification of the constitutive properties of the laminated core when the induction motor rotates.

2 Finite-element model

The finite-element model is based on the Timoshenko beam theory described in [23] in which N_e is the number

of finite-elements of the model comprising n_δ d.o.f. included in the set Σ such that $n_\delta = 4\,(N_e + 1)$. The general equation of motion of a rotor after performing the usual Lagrange equations is written as follows [24]:

$$M\ddot{\delta} + C\dot{\delta} + K\delta = F^{\text{ext}}\,(t) \tag{1}$$

where $\delta \in \mathbb{R}^{n_\delta}$ is a vector dependent on time t storing all the nodal displacements, $\dot{(\,)}$ and $\ddot{(\,)}$ respectively stand for the first and second time derivatives, $M \in \mathscr{M}_{n_\delta,n_\delta}$ is a symmetric global mass matrix, $C \in \mathscr{M}_{n_\delta,n_\delta}$ is a non symmetric matrix, a function of the speed of rotation, including the gyroscopic effect and the usual non symmetric damping characteristics of the bearings. $K \in \mathscr{M}_{n_\delta,n_\delta}$ is the global stiffness matrix including the stiffness effects of the bearings and $F^{\text{ext}}\,(t) \in \mathbb{R}^{n_\delta}$ is the vector including the external forces applied to the rotor including those due to gravity, unbalance effects and asynchronous forces.

This article focuses on the dynamics of induction motor rotors at standstill in order to identify the constitutive properties of magnetic laminated cores since it is represents an important unknown factor when predicting the dynamics of such structures. An in-plane non rotating modal analysis ($n_\delta = 2\,(N_\text{e} + 1)$) was therefore performed by considering the associated conservative system of the rotor. Thus Equation (1) is written as:

$$M\ddot{\delta} + K\delta = 0 \tag{2}$$

Given the monolithic character of the structure, the shear and rotation inertia effects (Rayleigh effects) are taken into account in each finite-element of the Timoshenko beam that contains two d.o.f. per node: a lateral displacement v and a rotation θ. Let Ω be the union of all the elements $\mathscr{K}$ of the mesh:

$$\Omega = \bigcup_{e=1}^{N_e} \mathscr{K}_e \tag{3}$$

where N_e is the total number of elements and ${}^e(\,)$ is the exponent associated with an element $\mathscr{K}_\text{e}$. A element $\mathscr{K}_e$ is therefore associated with four dof: $\{v_\text{e}, \theta_\text{e}, v_{\text{e}+1}, \theta_{\text{e}+1}\}$. An elementary stiffness matrix can be expressed as follows:

$${}^eK = {}^eK_\text{f} + {}^eK_\text{G} \tag{4}$$

where ${}^eK_\text{f} \in \mathscr{M}_{4,4}$ is the elementary matrix of the elastic stiffness defined by Equation (A.1) and [25]. An elementary cross section correction coefficient ${}^ek$ is defined by Equation (A.3) and [26]. Matrix ${}^eK_\text{G} \in \mathscr{M}_{4,4}$ is the elementary geometric stiffness matrix due to axial force ${}^eF_N$, Equation (A.4), (see Annexe A).

An elementary mass matrix can be written as follows:

$${}^eM = {}^eM_v + {}^eM_\theta \tag{5}$$

The first term of the second member ${}^eM_v \in \mathscr{M}_{4,4}$, Equation (B.1), is due to the translation effect of the cross section. Equation (B.2) is the expression of the second term ${}^eM_\theta \in \mathscr{M}_{4,4}$ due to the effects of rotation of the cross section, generally neglected for slender structures.

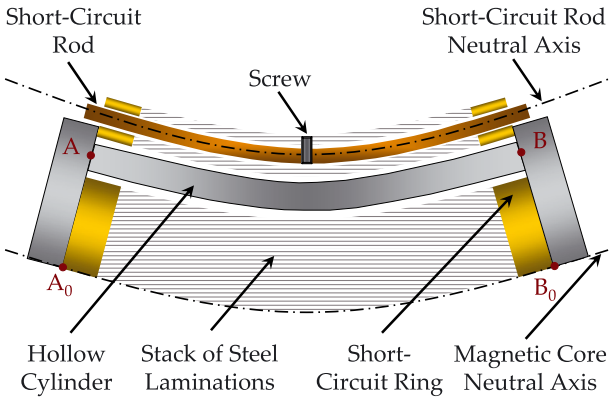

Fig. 2. Kinematic assumptions.

When updating finite-elements models, it is advisable to have an accurate model of the real structure, both geometrically and phenomenologically. The complexity of the structure of the magnetic mass must therefore be described with precision in order to identify the properties of the elements that compose it. Therefore to identify the constitutive properties of the laminated core, hypotheses are required to model the tie rods and the short circuit rods. The task of modeling them is based on beams whose neutral lines coincide with the neutral line of the laminated core. The beams of the short circuit bars are screwed on the laminated core via their centers (see Fig. 2); their ends can therefore move in the short-circuit rings. The beams of the tie rods are modeled as a single finite-element equivalent cylinder connected to nodes A_0 and B_0 (see Fig. 2). Let d_ti^ext and d_ti^int be the inner and outer diameters respectively calculated as follows:

$$d_\text{ti}^\text{ext} = \left(\frac{8I_{G_{y_\text{ti}}}}{S_\text{ti}} + \frac{2S_\text{ti}}{\pi}\right)^{\frac{1}{2}}, \quad d_\text{ti}^\text{int} = \left(\frac{8I_{G_{y_\text{ti}}}}{S_\text{ti}} - \frac{2S_\text{ti}}{\pi}\right)^{\frac{1}{2}} \tag{6}$$

where S_ti and $I_{G_{y_\text{ti}}}$ are the cross section and second moment of inertia of the N_ti tie rods respectively:

$$S_\text{ti} = N_\text{ti}\frac{\pi}{4}d_{ti}^2,$$

$$I_{G_{y_\text{ti}}} = N_\text{ti}\frac{\pi}{32}d_\text{ti}^4 + S_\text{ti}e_\text{ti}^2 \overbrace{\sum_{i=0}^{N_\text{ti}-1} \sin^2\left(\frac{2\pi i}{N_\text{ti}}\right)}^{\frac{1}{2}N_\text{ti}} \tag{7}$$

The periphery of the short-circuit rings, the laminated core and shaft-ends are perforated to permit the insertion of the short-circuit rods and tie rods. Equation (6) is then used to model their cross sections. The traction prestress is modeled by the geometric stiffness matrix ${}^eK_\text{G}$ for the finite element of the cylinder.

3 Condensed modal functional

Let us assume that the finite element model presented in Section 2, Equation (2), depends on n unknown parameters $\{x_p\}_{p=1\ldots n}$, inherent to the stack of lamination, that

have to be identified in order to ensure that the model predicts correctly. Its parameters are identified by iterative minimization of a functional that expresses the difference between the predicted and measured quantities.

3.1 Definition

Let $\omega_k,\ \hat{\omega}_k \in \mathbb{R}$ be the predicted and measured natural frequency respectively and $\varphi_k \in \mathbb{R}^{n_\delta}$ and $\hat{\varphi}_k \in \mathbb{R}^{n_c}$ be their associated mode shapes where $n_c \leq n_\delta$ represents the number of experimental measurement points included in the set $\Sigma_u,\ \Sigma_u \subset \Sigma$. Quantities ω_k and φ_k are obtained by calculating the harmonic solution of Equation (2):

$$(K - \lambda_k M)\,\varphi_k = 0 \quad \text{with} \quad \lambda_k = \omega_k^2, \quad k = 1, \ldots, m \tag{8}$$

where $\lambda_k \in \mathbb{R}$ and m are the number of eigen-elements. The same problem can be written in a more compact form:

$$\mathscr{R}_k - \omega_k^2 = 0 \quad \text{with} \quad \mathscr{R}_k = \frac{\varphi_k^t K \varphi_k}{\varphi_k^t M \varphi_k} \tag{9}$$

where $\mathscr{R}_k \in \mathbb{R}$ denotes the Rayleigh quotient, the ratio of potential and kinetic energies of the kth mode shape. Therefore an exact correlation between the measured and predicted natural frequencies and mode shapes leads to $\varphi_k = \hat{\varphi}_k$ and $\omega_k^2 = \hat{\omega}_k^2$. Since a real correlation never occurs in real cases we propose to quantify the difference between the modal predicted and measured quantities by using an estimate (a residual) $\mathscr{E}$, which transforms Equation (9) into:

$$\mathscr{E}_k = 1 - \frac{1}{\hat{\omega}_k^2} \frac{\hat{\varphi}_k^t K \varphi_k}{\hat{\varphi}_k^t M \varphi_k}, \quad k = 1, \ldots, m \tag{10}$$

where $\mathscr{E}_k$ denotes the kth component of the modal error estimate $\mathscr{E} \in \mathbb{R}^m$.

The mode shapes φ_k are composed of lateral deflections and rotations of cross sections, whereas the measured mode shapes $\hat{\varphi}_k$ only comprise lateral deflections. A Guyan condensation can therefore relate the lateral displacement d.o.f. of the finite element model to the measured ones. By partitioning the vector δ of all the d.o.f. into n_c master d.o.f. δ_c for lateral deflections v and in n_i slave d.o.f. δ_i for the rotations of the cross sections θ [20], we obtain:

$$\delta = (\delta_i, \delta_c)^t \tag{11a}$$

$$\delta = \tilde{\psi} \delta_c \tag{11b}$$

where $\tilde{\psi} \in \mathscr{M}_{n_c, n_\delta}$ is the transformation matrix, Equation (2), obtained by partitioning the stiffness matrix of Equation (8):

$$K = \begin{bmatrix} K_{ii} & K_{ic} \\ K_{ci} & K_{cc} \end{bmatrix} \tag{12a}$$

$$\tilde{\psi} = [\tilde{\varphi}^c, I]^t \tag{12b}$$

$$\tilde{\varphi}^c = -K_{ii}^{-1} K_{ic} \tag{12c}$$

where $I \in \mathscr{M}_{n_c, n_c}$ is an identity matrix and $\tilde{\varphi}^c \in \mathscr{M}_{n_i, n_c}$ is the matrix of the constraint modes obtained by neglecting all the nodal inertia forces of the slave d.o.f. The eigenvalue problem of the condensed model is therefore written as:

$$\left(\tilde{K} - \tilde{\lambda}_k \tilde{M}\right) \tilde{\varphi}_k = 0 \tag{13a}$$

$$\tilde{M} = \tilde{\psi}^t M \tilde{\psi} \tag{13b}$$

$$\tilde{K} = \tilde{\psi}^t K \tilde{\psi} \tag{13c}$$

where $\tilde{\lambda}_k \in \mathbb{R}$, $\tilde{\varphi}_k \in \mathbb{R}^{n_c}$ and $\tilde{M},\ \tilde{K} \in \mathscr{M}_{n_c, n_c}$ are respectively the n_c eigen-values and eigen-vectors of the condensed finite-element model and the condensed mass and stiffness matrices. The modal estimate $\mathscr{E}$ therefore results from a combination of the predicted and measured mode shapes and natural frequencies so as to define a condensed modal functional f, so that:

$$f = \frac{1}{2} \sum_{k=1}^{m} \mathscr{E}_k^2 \tag{14}$$

with

$$\mathscr{E}_k = 1 - \frac{\mathscr{R}_k^*}{\hat{\omega}_k^2} \quad \text{such as} \quad \mathscr{R}_k^* = \frac{\hat{\varphi}_k^t \tilde{K} \tilde{\varphi}_k}{\hat{\varphi}_k^t \tilde{M} \tilde{\varphi}_k} \tag{15}$$

where $\mathscr{R}_k^* \in \mathbb{R}$ is the hybrid Rayleigh quotient. Thus each term $\mathscr{E}_k$ combines an experimental natural frequency and its associated mode shape in an adimensional term. The mode shapes do not need to be signed and it is not necessary to use weighting coefficients since the $\mathscr{E}_k$ have the same order of magnitude. The condensed modal error estimate $\mathscr{E}$ is therefore mainly based on the difference of the predicted and measured mode shapes in order to get the hybrid Rayleigh quotients $\mathscr{R}_k^*$ to tend to the exclusively experimental reference values, i.e. the measured natural frequencies $\hat{\omega}_k$.

3.2 Convergence

It was possible to define a still more hybrid estimate $\mathscr{F}$ by using the predicted natural frequencies $\tilde{\omega}_k$, defined such that $\tilde{\lambda}_k = \tilde{\omega}_k^2$, so that they participate in the identification process. This yields to:

$$\mathscr{F}_k = 1 - \frac{\mathscr{R}_k^*}{\hat{\omega}_k \tilde{\omega}_k}, \quad k = 1, \ldots, m \tag{16}$$

On the other hand, in the neighbourhood $\hat{x}$ of optimum x^* such as:

$$\hat{x} = (1 + \varepsilon)\, x^*, \quad \varepsilon \in \mathbb{R}^{+*}, \quad \varepsilon \ll 1 \quad \text{such as} \quad f(x^*) = 0 \tag{17}$$

where ε is a perturbation [27], we obtain:

$$\tilde{\varphi}_k(\hat{x}) = \hat{\varphi}_k + \varepsilon Y, \ Y \in \mathbb{R}^{n_c}, \ \frac{\|Y\|_2}{\|\hat{\varphi}_k\|_2} \leq 1, \ k = 1, \ldots, m \tag{18}$$

and

$$\mathscr{R}_k^* (\hat{x}) = \tilde{\omega}_k^2 (\hat{x}), \quad k = 1, \ldots, m \tag{19a}$$

$$\tilde{\omega}_k (\hat{x}) = \hat{\omega}_k (1 + \varepsilon), \quad k = 1, \ldots, m \tag{19b}$$

where Y is an arbitrary vector and $\| \cdot \|_2$ symbolizes the Euclidian norm. It is possible to establish the first elements of reflection relating to functional f by considering the estimators $\mathscr{E}$ and $\mathscr{F}$. By substituting Equations (19a) and (19b) in Equations (15) and (16) as well as their first and second derivatives, we obtain the values, Equations (20a), (20b), and first derivatives, Equations (21a), (21b), and second derivatives Equations (22a), (22b), of functionals $f(\mathscr{E})$ and $f(\mathscr{F})$ in the neighbourhood of x^*:

$$f(\mathscr{E})|_{\hat{x}} = 2m\varepsilon^2 + o(\varepsilon^3) \tag{20a}$$

$$f(\mathscr{F})|_{\hat{x}} = \frac{1}{2} m\varepsilon^2 \tag{20b}$$

$$\left.\frac{\partial f(\mathscr{E})}{\partial x_p}\right|_{\hat{x}} = 4\frac{m}{x_p^*}\varepsilon + o(\varepsilon^2) \tag{21a}$$

$$\left.\frac{\partial f(\mathscr{F})}{\partial x_p}\right|_{\hat{x}} = \frac{m}{x_p^*}\varepsilon \tag{21b}$$

$$\left.\frac{\partial^2 f(\mathscr{E})}{\partial x_p \partial x_q}\right|_{\hat{x}} = 4\frac{m}{x_p^* x_q^*} + o(\varepsilon) \tag{22a}$$

$$\left.\frac{\partial^2 f(\mathscr{F})}{\partial x_p \partial x_q}\right|_{\hat{x}} = \frac{m}{x_p^* x_q^*} \tag{22b}$$

Figure 3 shows the evolution of functionals $f(\mathscr{E})$ and $f(\mathscr{F})$, for the values of ε^2 between 10^{-6} and 10^{-2} and by considering an arbitrary vector Y. They have been calculated around an arbitrary reference value x_p by using the finite-element model shown in Figure 4 by considering the first six modes, i.e. $m = 6$. Their linear interpolations, plotted on a logarithmic scale, have the following forms:

$$\ln(f(\mathscr{E})) = 1.0003 \ln(\varepsilon^2) - 50.2044 \tag{23}$$

$$\ln(f(\mathscr{F})) = 1.0001 \ln(\varepsilon^2) - 51.5923 \tag{24}$$

Their slopes, both close to unity, corroborate the dependence in ε^2 of Equations (20a) and (20b). The expression of the ratios between the values, slopes and curvatures of functionals $f(\mathscr{E})$ and $f(\mathscr{F})$ demonstrates that in the neighbourhood $\hat{x}$ of optimum x^*:

$$\exists r \in \mathbb{R} \text{ such as } r \geq \left.\frac{f(\mathscr{E})}{f(\mathscr{F})}\right|_{\hat{x}} \geq \left.\frac{\frac{\partial f(\mathscr{E})}{\partial x_p}}{\frac{\partial f(\mathscr{F})}{\partial x_p}}\right|_{\hat{x}} \geq \left.\frac{\frac{\partial^2 f(\mathscr{E})}{\partial x_p \partial x_q}}{\frac{\partial^2 f(\mathscr{F})}{\partial x_p \partial x_q}}\right|_{\hat{x}} \geq 4 \tag{25}$$

Therefore although these functionals have a similar order of convergence in ε^2 in the neighbourhood of x^*, it can be seen clearly that the functional defined by Equation (14) is more sensitive and more convex if estimate $\mathscr{E}$, Equation (15), is preferred to estimator $\mathscr{F}$, Equation (16), because the curvature ratio of functionals $f(\mathscr{E})$ and $f(\mathscr{F})$ is greater than 4. Consequently, for a fixed convergence threshold, i.e. stopping criteria on the functional or its gradient, functional $f(\mathscr{E})$ will converge more fastly in a neighbourhood nearer the optimum x^* than functional $f(\mathscr{F})$ because the value and slope of the functional $f(\mathscr{E})$ are 4 times higher than those related to the functional $f(\mathscr{F})$. The ratio of the ordinates at the origin of the linear interpolations of functionals $f(\mathscr{E})$ and $f(\mathscr{F})$, plotted in Figure 3, shows, numerically, that a real r exists, Equation (25), so that:

$$r \geq \frac{\mathrm{e}^{-50.2044}}{\mathrm{e}^{-51.5923}} \geq \mathrm{e}^{1.3879} \geq 4.0064$$

4 Optimization strategy

The constitutive properties of the laminated core are defined by vector $x \in \mathbb{R}^n$ so that $\{x_p\}_{p=1\ldots n}$ where n is the number of optimization parameters defined a priori by the constitutive properties of a Timoshenko beam element, i.e. Young's modulus E, shear modulus G and Poisson ratio υ. The union of the elements representing the laminated core is defined by:

$$\Omega_u = \bigcup_{e=e_\mathrm{i}}^{e_f} \mathscr{K}_e, \quad \Omega_u \subset \Omega \tag{26}$$

where e_i, e_f represent the lower and upper bounds respectively of the domain containing the contiguous finite elements related to the optimization variables (see Fig. 4). Therefore elementary matrices ${}^eK_\mathrm{f}$, ${}^eM_\mathrm{v}$ and ${}^eM_\theta$, Equations (A.1), (B.1) and (B.2), related to element $\mathscr{K}_\mathrm{e}$, $e = e_\mathrm{i}, \ldots, e_\mathrm{f}$ depend on n optimization variables x_p. The optimization strategy consists in minimizing the difference between the predicted and measured modal quantities and is thus reduced to the minimization of the Euclidian norm of the condensed modal functional, Equation (15), also called global functional f, so that:

$$\text{Find } x \text{ such as } \min_{x \in \mathbb{R}^n} f(x) \quad \text{with} \quad f(x) = \frac{1}{2} \|\mathscr{E}(x)\|_2^2 \tag{27}$$

where f is the global error residual, x the vector containing the estimations of the constitutive properties of the magnetic core, $\| \cdot \|_2$ the Euclidian norm of the error vector $\mathscr{E}$ and m the number of eigen-elements considered in the optimization process.

4.1 Sensitivity, robustness and precision

The choice of optimization variables is based on a sensitivity study of the finite element model (see Fig. 4) performed by successively calculating the values of functional f on the intervals of the relative variations x_p^r of

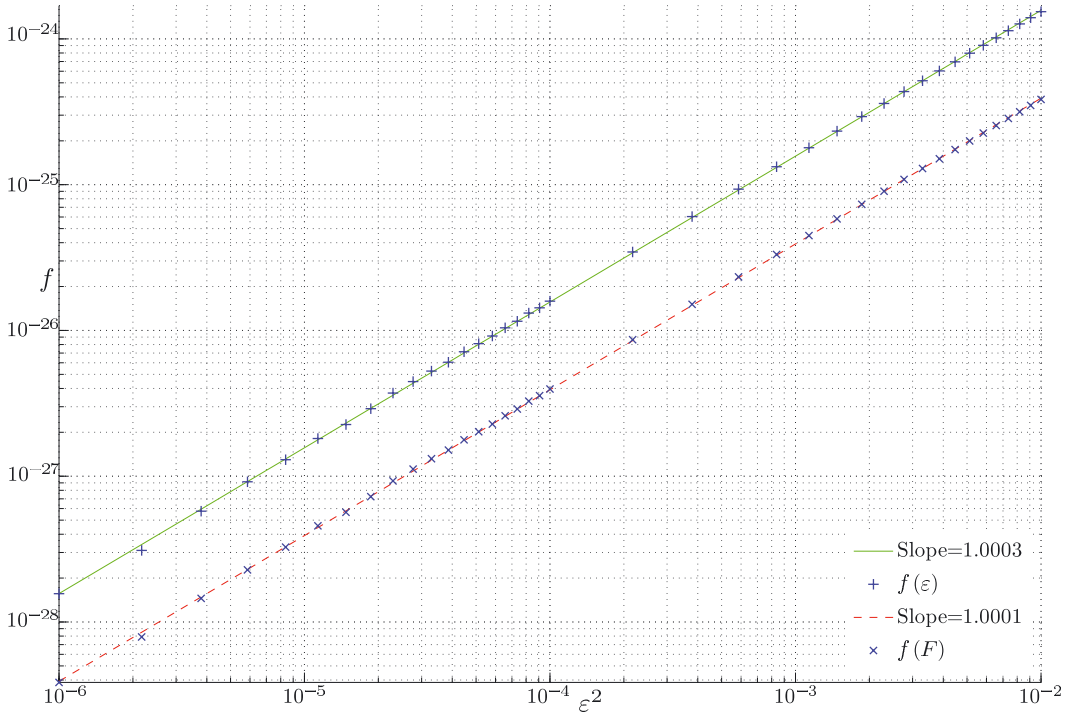

Fig. 3. Evolution of condensed modal functionals $f(\mathscr{E})$ (+) and $f(\mathscr{F})$ (×) as a function of the square of the perturbation ε. Their respective linear interpolations have the following equation: $\ln(f(\mathscr{E})) = 1.0003\ln(\varepsilon^2) - 50.2044$ (solid line, –) et $\ln(f(\mathscr{F})) = 1.0001\ln(\varepsilon^2) - 51.5923$ (dotted line, ––).

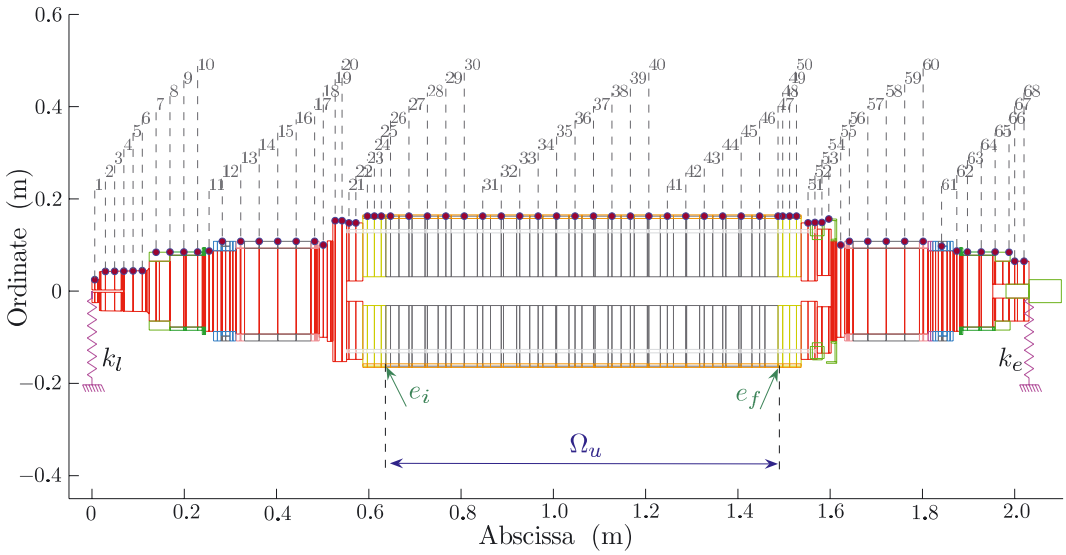

Fig. 4. Finite element model. The red dots (•) represent the experimental measurement points.

the constitutive properties of the stack defined by the Timoshenko theory, i.e. the Young's modulus E, shear modulus G and the Poisson coefficient υ. The relative variations x_p^r are defined in relation to an arbitrary reference configuration such that:

$$x_p^r = \frac{x_p}{x_{0p}},\ p = 1, \ldots, 3 \tag{28}$$

where $\{x_{01}, x_{02}, x_{03}\} = \{8 \times 10^{10}\ \text{N.m}^{-2},\ 3 \times 10^{10}\ \text{N.m}^{-2}, \frac{1}{3}\}$.

Figure 5 shows the evolution of components $\frac{1}{2}\mathscr{E}_k^2$ of global functional f on a range of ±50% of the relative values of optimization parameters x_p^r, $p = 1 \ldots 3$ by considering the first six modes, i.e. $k = 1, \ldots, 6$. The components of modal functional f are convex and only have

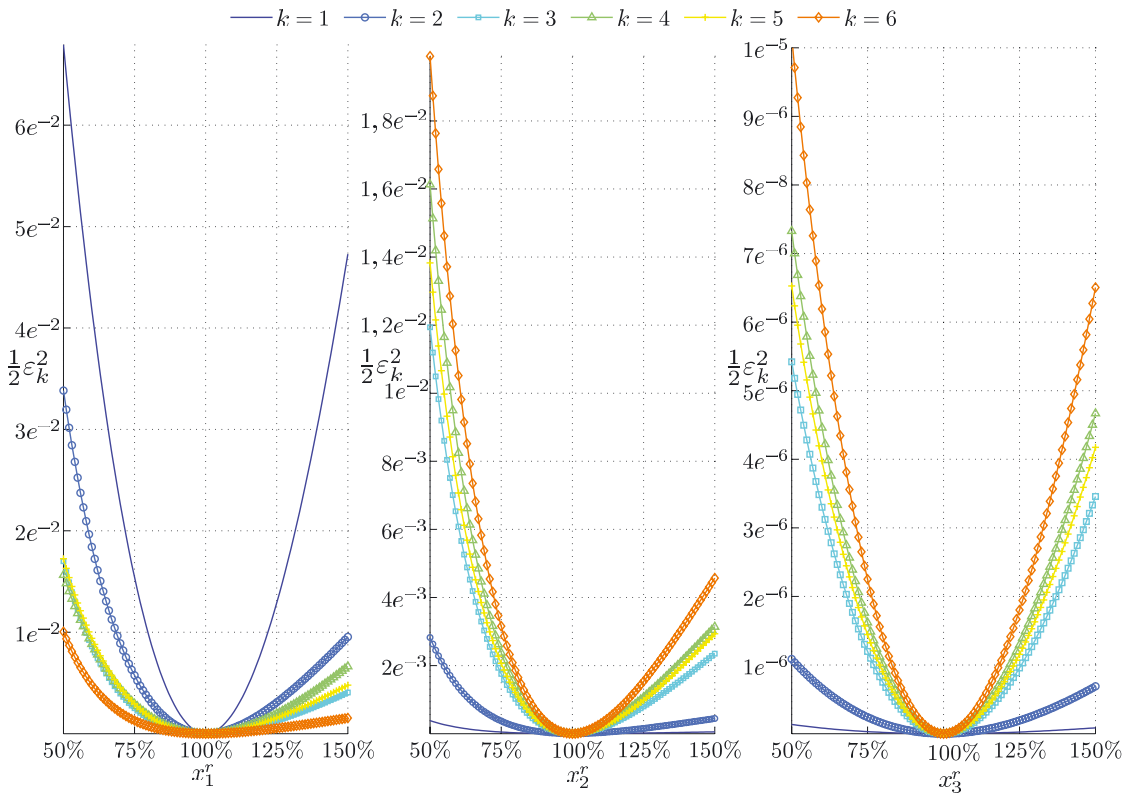

Fig. 5. Evolution of components $\frac{1}{2}\mathscr{E}_k^2$ of the condensed modal functional f on a range of ±50% of the relative values of optimization parameters x_p^r, $p = 1 \ldots 3$: Young's modulus (x_1^r), shear modulus (x_2^r) and Poisson ratio (x_3^r).

one local minimum in the range ±50% of values x_p^r which ensures the robustness of the optimization procedure independently of the initial estimation of the parameters to be identified. Furthermore, all of them converge to zero in the neighbourhood of the reference parameters x_p^r, thereby ensuring the good precision of the identification method since the residual identification error stems solely from experimental uncertainties.

The value of components $\frac{1}{2}\mathscr{E}_k^2$ is of order 10^{-1} and 10^{-2} for the relative variations of moduli E and G whereas it is only of order 10^{-6} for a relative variation of the coefficient υ. The sensitivity of the $\frac{1}{2}\mathscr{E}_k^2$ of modulus G (parameters x_2^r) clearly increases with the index of the mode, since the length of the wave of the bending mode shapes decreases concurrently.

The relative sensitivity of a component $\mathscr{E}_k$ in comparison to a parameter is then calculated for each parameter x_p^r, and for each mode k:

$$\frac{\partial \mathscr{E}_k}{\partial x_p^r} \cong \frac{\Delta \mathscr{E}_k}{\Delta x_p^r} = \frac{\mathscr{E}_k\left(x_p\right) - \mathscr{E}_k\left(x_{0p}\right)}{x_p^r - 1}, \quad p = 1, \ldots, n \qquad (29)$$

The values of the relative sensitivities are presented in Table 1. The relative sensitivities are of order 10^{-1} for the relative variations of moduli E and G whereas it is of the order 10^{-3} for a relative variation of the coefficient υ. This means that the modulus is not very sensitive to the Poisson ratio of the laminated core and that the Young and shear moduli are dominant parameters. Also G is specified as being independent of E and υ in the presence of anisotropy [6]. Therefore the x_p, are defined by the doublet $\{E, G\}$.

Table 1. Sensitivity of components $\mathscr{E}_k$ of modal functional f as a function of the relative values x_p^r equal to 1% of the Young and shear moduli and Poisson ratio, indicated in the 1st, 2nd and 3rd columns respectively.

k	$p = 1$	$p = 2$	$p = 3$
1	6.69×10^{-1}	2.97×10^{-2}	9.15×10^{-4}
2	3.61×10^{-1}	8.47×10^{-2}	2.61×10^{-3}
3	2.32×10^{-1}	1.89×10^{-1}	5.83×10^{-3}
4	2.74×10^{-1}	2.20×10^{-1}	6.78×10^{-3}
5	2.57×10^{-1}	2.08×10^{-1}	6.41×10^{-3}
6	1.57×10^{-1}	2.60×10^{-1}	7.99×10^{-3}

4.2 Minimization algorithm

Let x^i be the vector of n (in this case, $n = 2$) optimization variables x at iteration i. The x^i are defined with respect to the initial optimization variables x^0 in order to avoid possible numerical conditioning problems in the minimization algorithm, especially in the calculation of Jacobian matrix $J \in \mathscr{M}_{m,n}$, Equation (32). In addition, to ensure boundaring the optimization variables

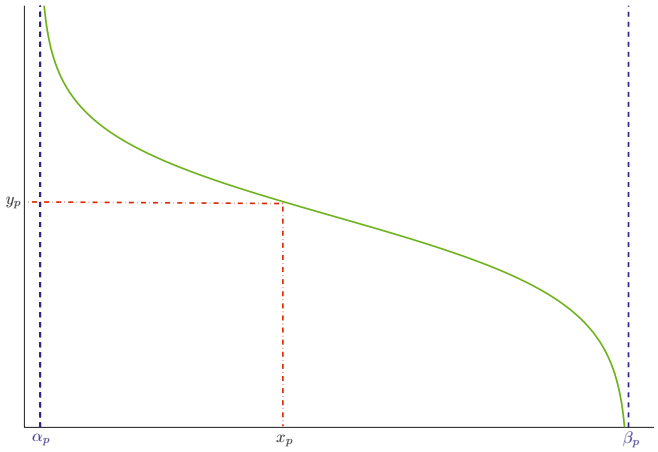

Fig. 6. View of the bijection σ, Equation (30), used to bound the optimization variables x_p. The value of parameter χ was set at $\frac{5}{100}$.

x_p (for example, the need to obtain positive constitutive properties), we propose using the following bijection:

$$\sigma : y_p \mapsto x_p = \alpha_p + \frac{(\beta_p - \alpha_p)}{1 + \mathrm{e}^{\chi y_p}}, \quad y_p, \chi \in \mathbb{R}, \\ x_p \in [\alpha_p, \beta_p], \quad p = 1, \ldots, n \tag{30}$$

where χ is a parameter closely related to the value of the derivative of the bijection σ at $y_p = 0$, α_p and β_p are the values of the lower and upper bounds respectively of the domains of definition of variables x_p, so that:

$$\begin{cases} y_p \to -\infty, \ x_p \to \beta_p \\ y_p \to 0, \ x_p \to \frac{1}{2}(\alpha_p + \beta_p) \\ y_p \to +\infty, \ x_p \to \alpha_p \end{cases} \tag{31}$$

Using this type of bijection (see Fig. 6) allows benefiting from the pros (simplicity of implementing) but not the cons (which generally requires higher calculation effort) of a constraint algorithm. Therefore the iterations are no longer necessary on the bounded x_p variables but on the variables $y_p \in \mathbb{R}$. The optimization problem therefore amounts to solving the following problem:

$$\begin{cases} \min\limits_{x \in \mathbb{R}^n} f(x) \\ \text{with } f(x) = \frac{1}{2} \sum\limits_{k=1}^{m} \mathscr{E}_k^2(x) \\ \text{with contraints} \\ \alpha_p < x_p < \beta_p, \quad p = 1, \ldots n \end{cases}$$

Functional f is therefore minimized by using the Levenberg-Marquardt algorithm which is especially robust for least squares type functionals:

$$\left| \begin{array}{l} x^0, \quad y^0 = \sigma^{-1}(x^0), \quad \mu^0 \in \mathbb{R} \text{ given} \\ x^i = \sigma(y^i) \\ f(x^i) = \frac{1}{2} \sum\limits_{k=1}^{m} \mathscr{E}_k^2(x^i) \\ \gamma^i = -\left(H^i(x^i) + \mu^i I\right)^{-1} \nabla f(x^i) \\ y^{i+1} = y^i + \tau^i \gamma^i \end{array} \right.$$

$$\text{with} \quad \left| \begin{array}{l} J_{kp}(x^i) = \frac{\partial \mathscr{E}_k}{\partial y_p^i} = \frac{\partial \mathscr{E}_k}{\partial x_p^i} \frac{\partial x_p^i}{\partial y_p^i} \\ \nabla f(x^i) = J(x^i)^t \mathscr{E}(x^i) \\ H^i \cong J(x^i)^t J(x^i) \end{array} \right. \tag{32}$$

where I, $H^i \in \mathscr{M}_{n,n}$ are the approximated identity and Hessian matrices respectively, and $\nabla f \in \mathbb{R}^n$ represents the gradient of the functional f.

The robustness of this algorithm stems from the fact that if $\mu^i \to \infty$, the algorithm tends to the steepest descent method whose order of convergence is equal to one. On the contrary, if $\mu^i \to 0$, the algorithm tends to the Gauss-Newton method whose order of convergence is equal to two, thereby highlighting the algorithm's efficiency. The (Marquardt) damping parameter μ^i is updated by calculating a "gain factor", i.e. the ratio between the decrease of the functional $f(x^i)$ and its approximation obtained by developing the vector $\mathscr{E}(x^i)$ into a first order Taylor series. The descent step τ^i can be obtained by using a line search algorithm. We prefer the method proposed in [28] by stipulating $\tau^i = 1$ and by frequently updating parameter μ^i. This leads to smoother and faster convergence than the method initially proposed by Marquardt [29].

4.3 Eigen-element derivative

The Jacobian matrix of vector $\mathscr{E}(x^i)$ implicitly depends on eigen-elements. Let us consider Equation (1) which assumes that the eigen-vectors $\tilde{\varphi}$ are normalized with respect to the condensed mass matrix $\tilde{M}$:

$$\tilde{\varphi}_k^t \tilde{M} \tilde{\varphi}_k = 1, \quad k = 1, \ldots, m \tag{33}$$

By deriving Equations (1) and (33) with respect to x_p, the eigen-vectors derivatives then become governed by [16]:

$$\tilde{A}_k \frac{\partial \tilde{\varphi}_k}{\partial x_p} = \tilde{P}_k, \quad A_k \in \mathscr{M}_{n_c,n_c}, \ \tilde{P}_k \in \mathbb{R}^{n_c} \tag{34}$$

$$\tilde{\varphi}_k^t \tilde{M} \frac{\partial \tilde{\varphi}_k}{\partial x_p} = \tilde{Q}_k, \quad \tilde{Q}_k \in \mathbb{R} \tag{35}$$

where

$$\tilde{Q}_k = -\frac{1}{2} \tilde{\varphi}_k^t \frac{\partial \tilde{M}}{\partial x_p} \tilde{\varphi}_k, \quad \tilde{A}_k = \left(\tilde{K} - \tilde{\lambda}_k \tilde{M}\right), \\ \tilde{P}_k = -\left(\frac{\partial \tilde{K}}{\partial x_p} - \frac{\partial \tilde{\lambda}_k}{\partial x_p} \tilde{M} - \tilde{\lambda}_k \frac{\partial \tilde{M}}{\partial x_p}\right) \tilde{\varphi}_k$$

By premultiplying Equation (34) by $\tilde{\varphi}_k^t$ and by combining Equations (1) and (33), the derivative of the kth eigenvalue $\tilde{\lambda}_k$ with respect to x_p is obtained by the following relation:

$$\frac{\partial \tilde{\lambda}_k}{\partial x_p} = \tilde{\varphi}_k^T \left(\frac{\partial \tilde{K}}{\partial x_p} - \tilde{\lambda}_k \frac{\partial \tilde{M}}{\partial x_p} \right) \tilde{\varphi}_k \tag{36}$$

Regarding the derivatives of the eigen-values, the problem is that Equation (34) is not invertible. Indeed, matrix $\tilde{A}_k$ is singular and of rank $n_c - 1$ as $\tilde{\lambda}_k$ is a eigenvalue of Equation (1) whose multiplicity is equal to 1. The modal method assumes that the derivative of the kth eigen-vector with respect to x_p can be expressed as follows:

$$\frac{\partial \tilde{\varphi}_k}{\partial x_p} = \sum_{j=1}^{n_c} \tilde{c}_j \tilde{\varphi}_j \quad \text{with} \quad \tilde{c}_j = \frac{\tilde{\varphi}_j^t \tilde{P}_k}{\tilde{\lambda}_j - \tilde{\lambda}_k}, j \neq k \tag{37}$$

where $\tilde{c}_j \in \mathbb{R}$ are obtained by substituting Equation (37) in Equation (34) and by premultiplying by $\tilde{\varphi}_k^t$. Equation (37) shows that the partial derivative of the kth eigen-vector has a unique expression as a linear combination of all the eigen-vectors of the model, with the exception of the kth:

$$\frac{\partial \tilde{\varphi}_k}{\partial x_p} = \sum_{\substack{j=1 \\ j \neq k}}^{n_c} \tilde{c}_j \tilde{\varphi}_j + \tilde{c}_k \tilde{\varphi}_k \equiv \tilde{V}_k + \tilde{c}_k \tilde{\varphi}_k$$
$$\text{with} \qquad \tilde{c}_k = \tilde{Q}_k - \tilde{\varphi}_k \tilde{M} \tilde{V}_k, \quad V_k \in \mathbb{R}^{n_c} \tag{38}$$

where $\tilde{c}_k$ is obtained by substituting Equation (38) in Equation (35). This method, which is costly in computer time, requires knowledge of all the eigen-vectors of the model. By substituting Equation (38) in Equation (34), Nelson [18] proposes to remove the singularity of matrix $\tilde{A}_k$ by cancelling a component of vector $\tilde{V}_k$, therefore Equation (34) becomes invertible and the homogenous solution is obtained. The complete solution is given by Equation (38). This method requires as many inversions of matrix $\tilde{A}_k$ as derivatives desired. The derivatives of the eigen-elements require knowledge of the derivatives of the condensed matrices obtained by using the derivative of $\tilde{\psi}$, Equation (11b):

$$\frac{\partial \tilde{\psi}}{\partial x_p} = \left[\frac{\partial \tilde{\varphi}^c}{\partial x_p}, 0 \right]^t \quad \text{with} \quad \frac{\partial \tilde{\varphi}^c}{\partial x_p} = -K_{ii}^{-1} \left(\frac{\partial K_{ic}}{\partial x_p} - \frac{\partial K_{ii}}{\partial x_p} \tilde{\varphi}^c \right) \tag{39}$$

where $\frac{\partial \tilde{\varphi}^c}{\partial x_p}$ is the derivative of the matrix of the constraint modes (Eq. (3)). The derivatives of the condensed stiffness and mass matrices are therefore:

$$\frac{\partial \tilde{K}}{\partial x_p} = \tilde{\psi}^t \frac{\partial K}{\partial x_p} \tilde{\psi} + 2 \tilde{\psi}^t K \frac{\partial \tilde{\psi}}{\partial x_p} \tag{40}$$

and

$$\frac{\partial \tilde{M}}{\partial x_p} = \tilde{\psi}^t \frac{\partial M}{\partial x_p} \tilde{\psi} + 2 \tilde{\psi}^t M \frac{\partial \tilde{\psi}}{\partial x_p} \tag{41}$$

where each term depends explicitly on the elementary stiffness and mass matrices defined in Equations (A.1), (B.1) and (B.2). Finally, the J_{kp} components of the Jacobian matrix, Equation (32) are written as follows:

$$J_{kp} = \frac{\partial \mathscr{E}_k}{\partial x_p} \quad \text{with} \quad k = 1, \ldots, m \quad \text{et} \quad p = 1, \ldots, n \tag{42}$$

with

$$\frac{\partial \mathscr{E}_k}{\partial x_p} = \frac{-1}{\hat{\varphi}_k^t \tilde{M} \tilde{\varphi}_k} \left[\left(\hat{\varphi}_k^t \frac{\partial \tilde{K}}{\partial x_p} \tilde{\varphi}_k + \hat{\varphi}_k^t \tilde{K} \frac{\partial \tilde{\varphi}_k}{\partial x_p} \right) - \frac{\hat{\varphi}_k^t \tilde{K} \tilde{\varphi}_k}{\hat{\varphi}_k^t \tilde{M} \tilde{\varphi}_k} \left(\hat{\varphi}_k^t \frac{\partial \tilde{M}}{\partial x_p} \tilde{\varphi}_k + \hat{\varphi}_k^t \tilde{M} \frac{\partial \tilde{\varphi}_k}{\partial x_p} \right) \right] \frac{1}{\hat{\omega}_k^2} \tag{43}$$

5 Industrial application

5.1 Experimental modal analysis

An experimental modal analysis is performed on a HSM rotor hanged vertically from a crane via a swivel hoist ring and a flexible sling (see Fig. 7). The experimental boundary conditions are close to free-free boundary conditions and taken into account by adding terms of low lateral stiffness applied to the end nodes of the rotor, Equation (44). The latter are calculated by considering the assembly composed of the rotor mass and the flexible sling (of negligible mass) as a double pendulum (see Fig. 8). After applying the theorem of unity displacement [23], the lateral stiffnesses are written as follows:

$$k_e = \frac{m_r g}{L_e}, \quad k_l = \frac{m_r g z_G}{(L_r^2 + z_G L_e)} \tag{44}$$

with k_l being the lateral stiffness at the end of the free end of the rotor, k_e the lateral stiffness of the flexible sling (see Fig. 4), m_r the total mass of the rotor, g the gravity acceleration, L_r the length of the rotor, z_G the center of the rotor mass and L_e the length of the flexible sling. The geometric characteristics are defined in Table 2. The rotor was excited radially along a meridian line with an impact hammer, and a force sensor measured the force transmitted to node $N°1$. To establish accurate mode shapes, the meridian line was discretized by 68 measurement points (see Fig. 4). The bandwidth considered ranged from 200 to 3200 Hz. The transfer functions were obtained by calculating the means (for three impacts) of ratios of Fourier transforms of temporal signals from the accelerometer and the force sensor. Magnitudes, shown in Figure 9, and the imaginary parts of the transfer functions, stemming from a dynamic analyzer, give the natural frequencies and mode shapes.

5.2 Identification

The model presented in Figure 4 is composed of the domain Ω so that $N_e = 175$, Equation (3), and the number of *dof* n_δ is equal to 352. Domain Ω_u containing

Fig. 7. Experimental set-up used during the modal analysis.

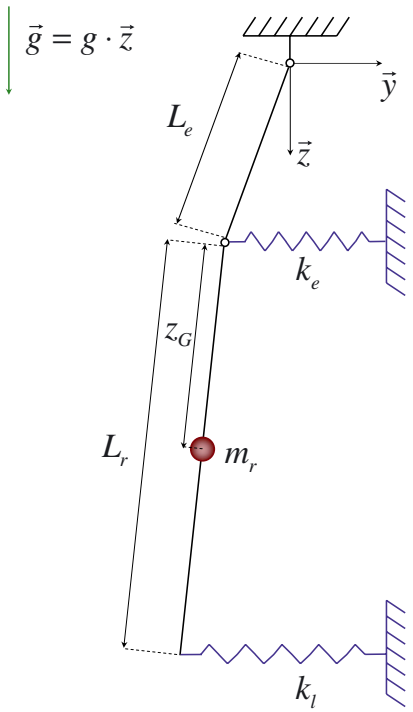

Fig. 8. Kinematic approximation relative to the rotor suspension set-up.

Table 2. Characteristics of the rotor.

Mass, m_r	998	kg
Length, L_r	2.03	m
Length, L_e	1.00	m
Center of mass, z_G	1.05940	m
Lateral stiffness, k_e	9.45×10^3	$\mathrm{N.m^{-1}}$
Lateral stiffness, k_l	1.93×10^3	$\mathrm{N.m^{-1}}$

the magnetic core is defined for $e_\mathrm{i} = 67$ and $e_\mathrm{f} = 116$, Equation (26).

The identification procedure was performed by varying the number m of the modes (natural frequencies and associated mode shapes) in the optimization algorithm so that $m = 2, \ldots, 6$. A minimum of two modes was chosen to ensure the uniqueness of the optimization problem. The Poisson ratio υ was set at 0.28, as in [7]. The optimization problem therefore contains two unknowns and the initial values of the optimization variables x^0, Equation (32) were set arbitrarily at $\left\{x_1^0 = 0.6 \times 10^{11},\ x_2^0 = 0.3 \times 10^{11}\right\} \left(\mathrm{N.m^{-2}}\right)$.

In [5–9, 11], the authors estimate and consider low Young and shear moduli values for the laminated core, slightly lower than those of steel. In order to satisfy this condition and also impose strictly positive optimization variables, the lower and upper bounds of the intervals containing the optimization variables x were defined as:

$$x_1 \in [\alpha_1, \beta_1]\,,\ x_2 \in [\alpha_2, \beta_2]$$

where

$$\begin{cases} \alpha_1 = \varepsilon, \beta_1 = 2.3 \times 10^{11} \\ \alpha_2 = \varepsilon, \beta_2 = \frac{\beta_1}{2(1+\upsilon)} \end{cases},\ \varepsilon \in R^{+*},\ \varepsilon \ll 1$$

Figure 10 shows the evolution of functional f, for $m = 6$ modes, during the optimization process that converged in $i = 13$ iterations to the optimum $\{x_1^*, x_2^*\}$, as indicated by the value of the norm of the gradient which is of order 10^{-9}. The evolution of the optimization variables during the minimization procedure is shown in Figure 11. The convergence time, less than 8 s, demonstrates the algorithm's rate of convergence, Equation (32), intrinsically linked to the evolution of Marquardt's damping parameter μ that shows a monotonous decrease during the minimization process and reaches a value equal to 10^{-8}. This behavior means that functional f is very close to a quadratic form of x for $x \in \left[x^0, x^*\right]$.

Figure 12 shows the evolution of relative successive iterations during the minimization procedure ($m = 6$) for different initial values of the parameters x^0. The range of variation of the initial values x^0 was set at $\pm 70\%$ of the optimal values $\{x_1^*, x_2^*\}$. The evolution of the iterations to a unique optimum demonstrates, numerically, the uniqueness of the solution of Equation (27) and the robustness of the algorithm, Equation (32).

Figure 13 shows the value of the mean global functional as a function of the number of modes m at the convergence of the algorithm. This magnitude is defined by the ratio between the quadratic functional $f\left(x^i\right)$, Equation (27), and the square of the number of modes m^2 so as to obtain a quantity that characterizes the mean difference between the predicted and measured modal quantities for each mode. The latter, plotted in Figure 13, decreases with the number of modes, meaning that the introduced finite element model is representative of the global dynamic of the rotor of interest. When more modes

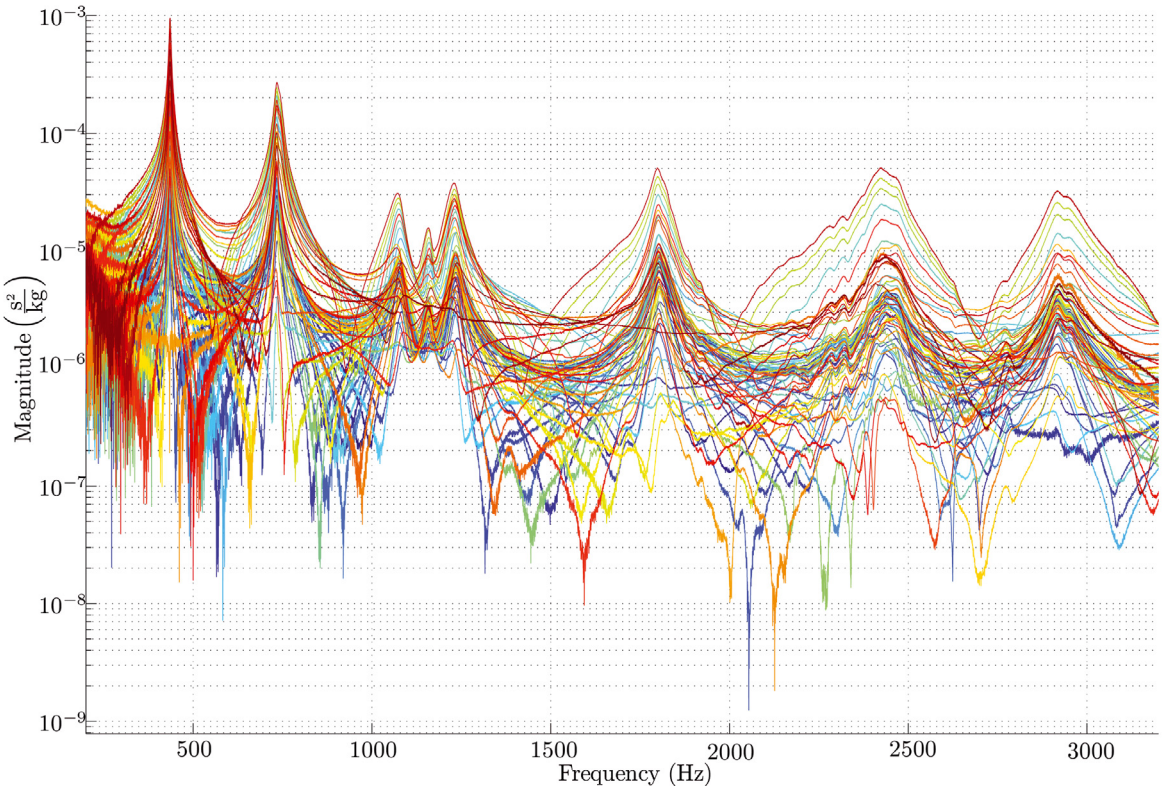

Fig. 9. Magnitudes of the transfer functions measured at the 68 points of the meridian line.

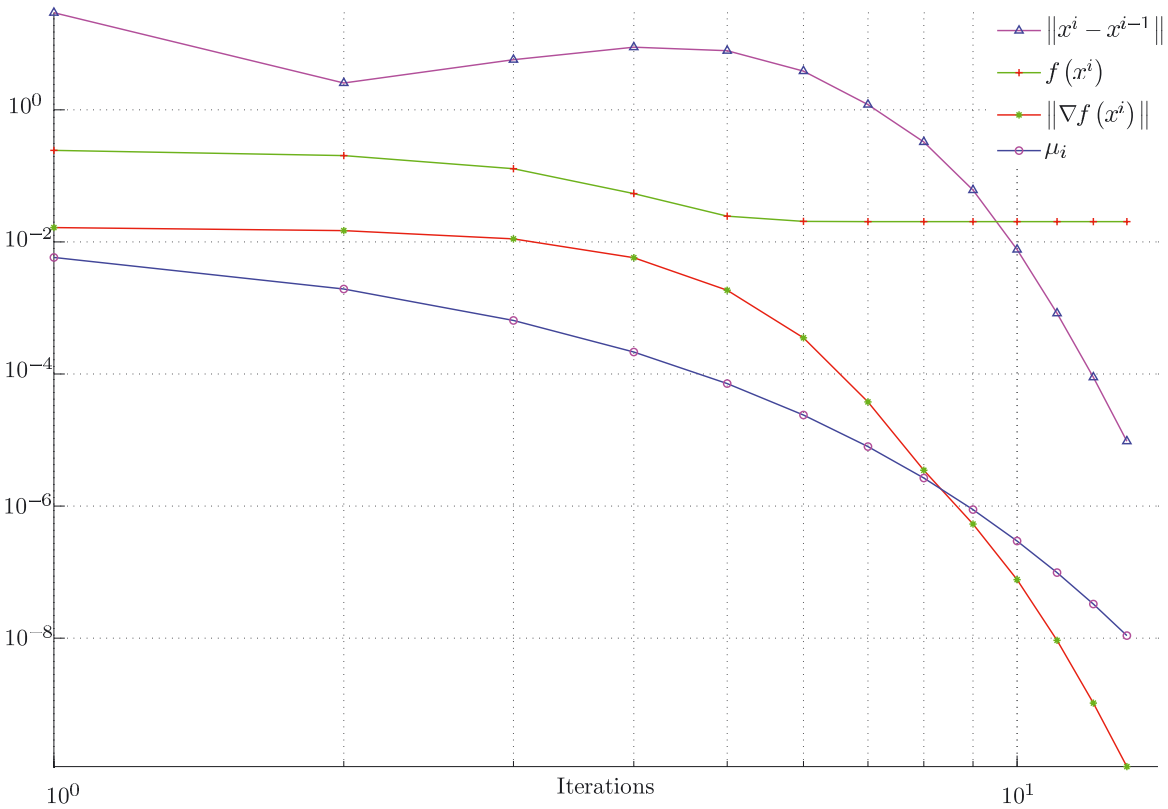

Fig. 10. Evolution of the norm of the differences between successive iterates (△), functional (+), norm of gradient (∗) and Marquardt damping parameter (○) during the iterations.

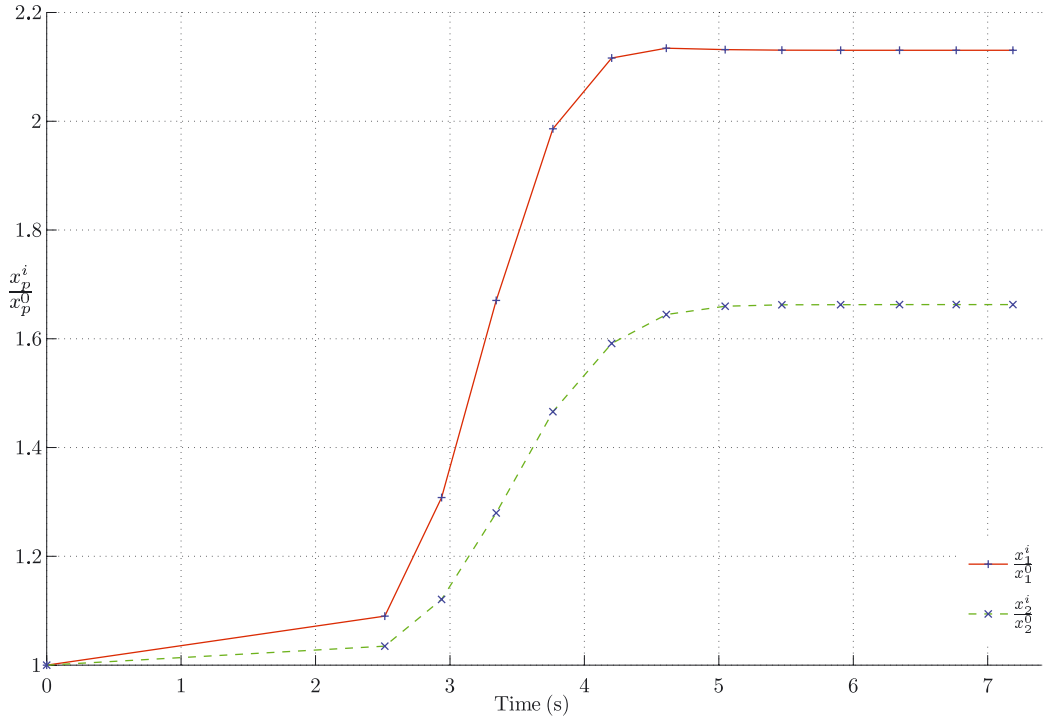

Fig. 11. Evolution of the relative values of the Young (+) and shear (×) moduli as a function of time (s) during the minimization.

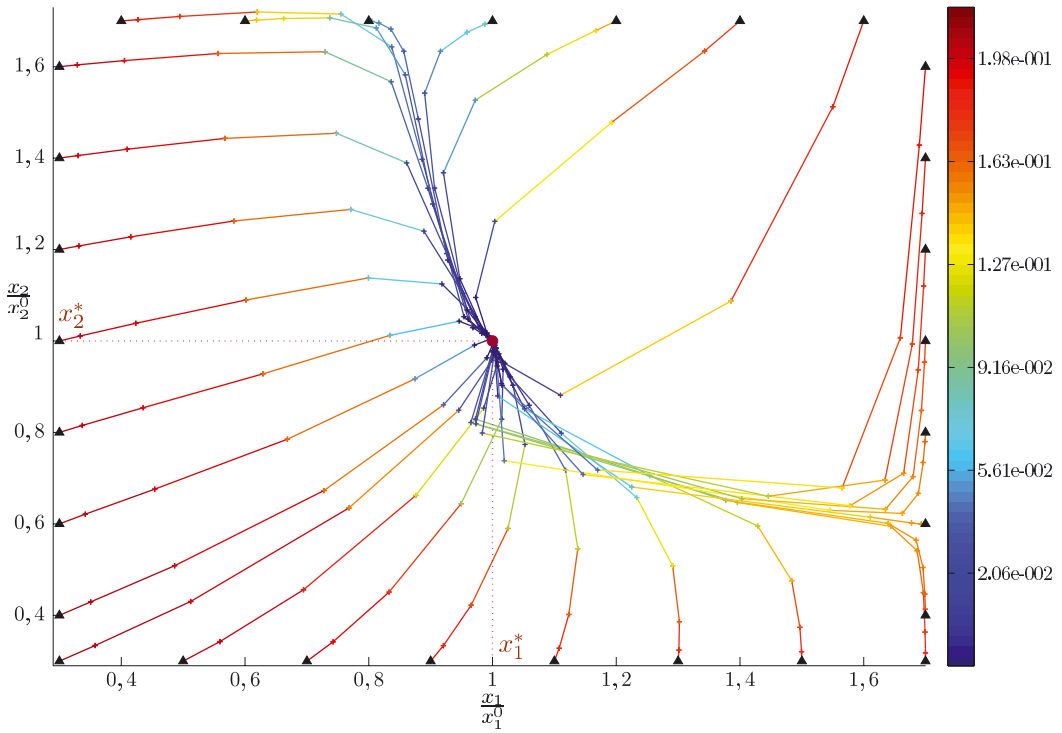

Fig. 12. Evolution of relative successive iterates (+) during the minimization procedure for different initial values of parameters x^0 (▲). The range of variation of the initial values x^0 is ±70% of the optimal values $\{x_1^*, x_2^*\}$ (●).

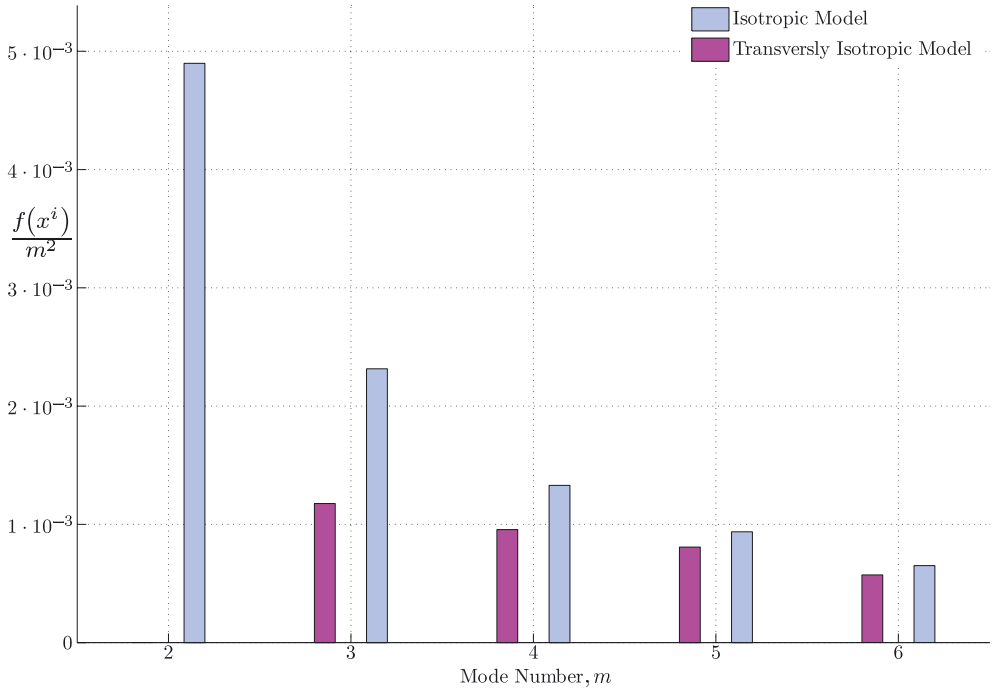

Fig. 13. Evolution of the mean global functional versus the number of modes.

Table 3. Values of the first six predicted and measured bending natural frequencies.

Mode	1	2	3	4	5	6
Measured (Hz)	435.55	735.16	1159.4	1802.0	2425.8	2918.4
Predicted (Hz)	418.86	796.78	1188.6	1781.8	2335.5	2889.1
Error (%)	−3.83	8.38	2.52	−1.12	−3.72	−1.00

Table 4. Values of the first six measured modal dampings.

Mode	1	2	3	4	5	6
Measured	6.008×10^{-3}	9.205×10^{-3}	1.592×10^{-2}	1.045×10^{-2}	1.935×10^{-2}	1.893×10^{-2}

are accounted for, the mean global functional features a monotonous convergence to a nonzero constant which represents the mean difference between a couple of predicted and measured mode. It is important that this quantity stabilizes and it should be noted that in [30], the authors consider distributions of transversely isotropic material along the laminated core axis, which if used here, would certainly make the mean global functional tend toward zero.

The number of modes also influences the values of the constitutive properties of the laminated core as shown in Figure 14. However, for this rotor, the parameters identified tend towards asymptotic values from five or more modes. Consequently, it is necessary to take into account enough modes, representative of the dynamic of the structure being studied, to identify relevant constitutive properties.

The same identification procedure was performed by considering the laminated core as an isotropic material, i.e. the shear modulus G is defined as a linear function of the Young's modulus E. The mean global energetic functional, plotted in Figure 13, is about 4.1% at 75% (for $m = 3, \ldots, 6$) higher than the mean global energetic functional obtained at the convergence of the optimization algorithm. Furthermore, Figure 14 shows that the asymptotic value of the shear modulus of the laminated core of the model is lower than that obtained with the isotropy assumptions. Therefore the identification procedure presented is more accurate than the classical methods considering restrictive hypotheses, such as isotropy, regarding the mechanical behavior of the laminated core.

The predicted natural frequencies and mode shapes were obtained by considering six modes in the identification procedure. Table 3 shows the six first predicted and measured natural frequencies while Figure 16 illustrates their associated mode shapes. The relative error between the predicted and measured natural frequencies is between 1.0% et 8.4% with an average of 3.6%.

Table 4 gives the modal dampings determined on the basis of transfer functions (see Fig. 9). The synthesis of the transfer functions are obtained on the basis of the constitutive properties identified for $m = 6$ modes and modal dampings. The synthesis of the magnitude and phase of the transfer function measured between nodes 19 and 1 is shown in Figure 15.

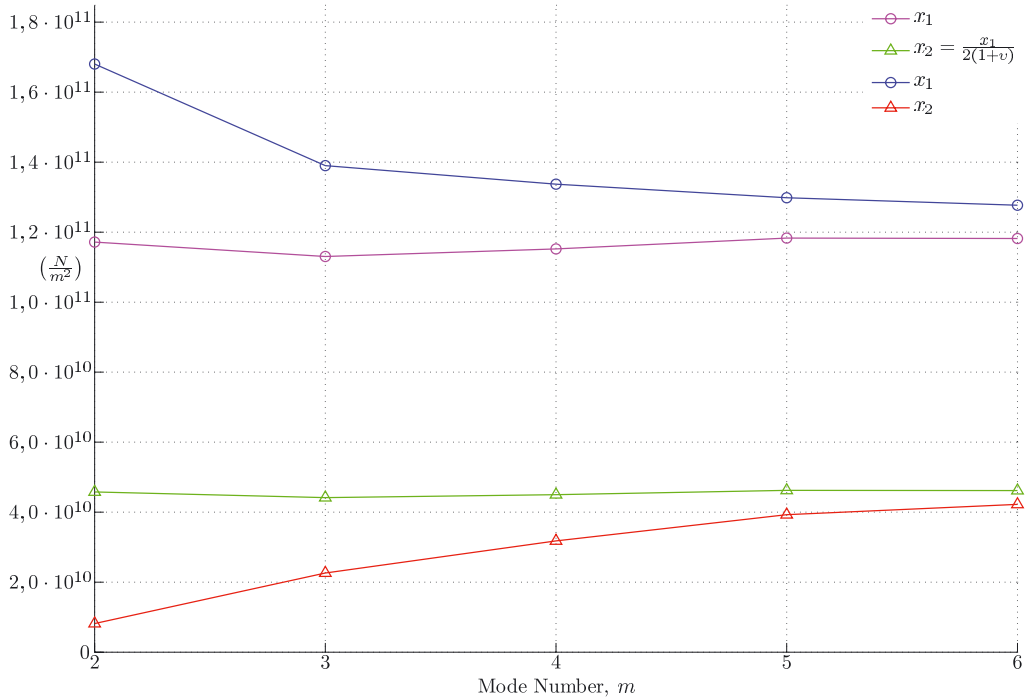

Fig. 14. Evolution of the Young E ($\bigcirc$, $\circ$ if isotropic) and shear G ($\triangle$, $\triangle$ if isotropic) moduli as a function of the number of modes considered in the identification procedure.

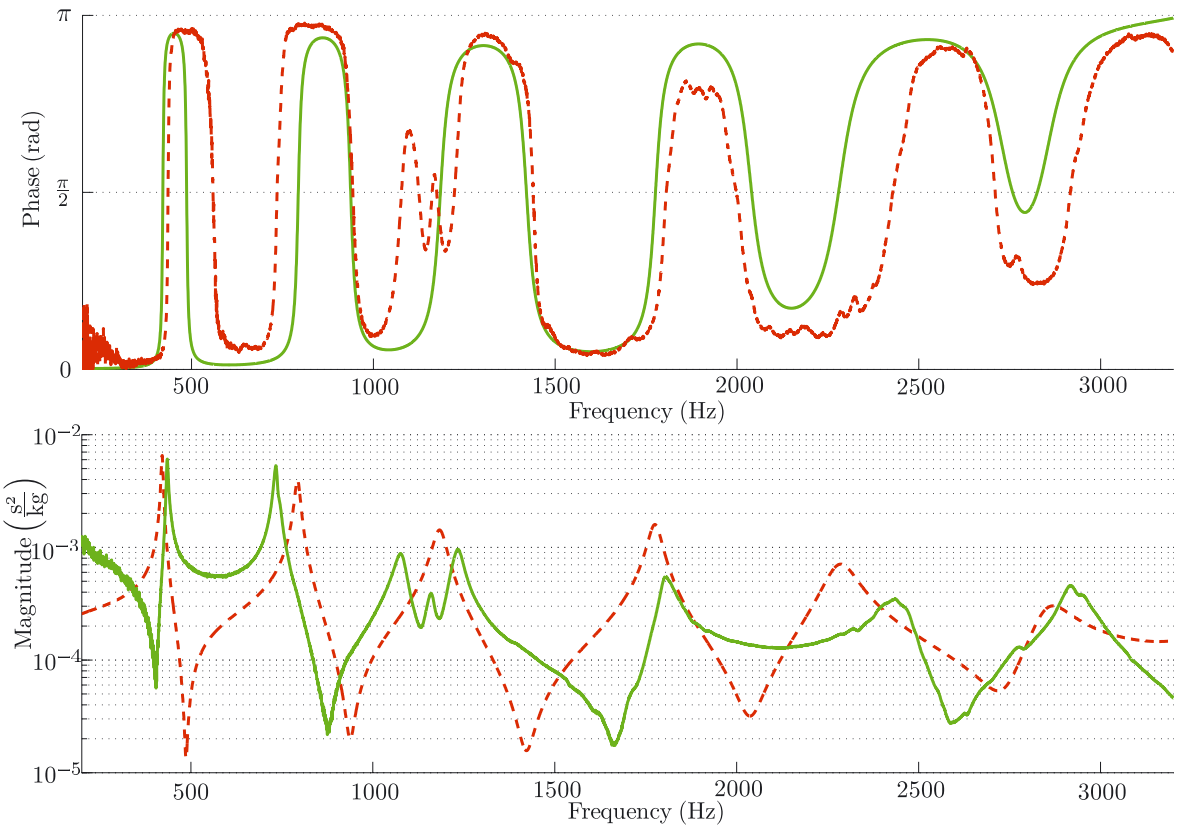

Fig. 15. View of the synthesis ($--$) of the magnitude and phase of a transfer function ($-$) measured between nodes $N°19$ and $N°1$.

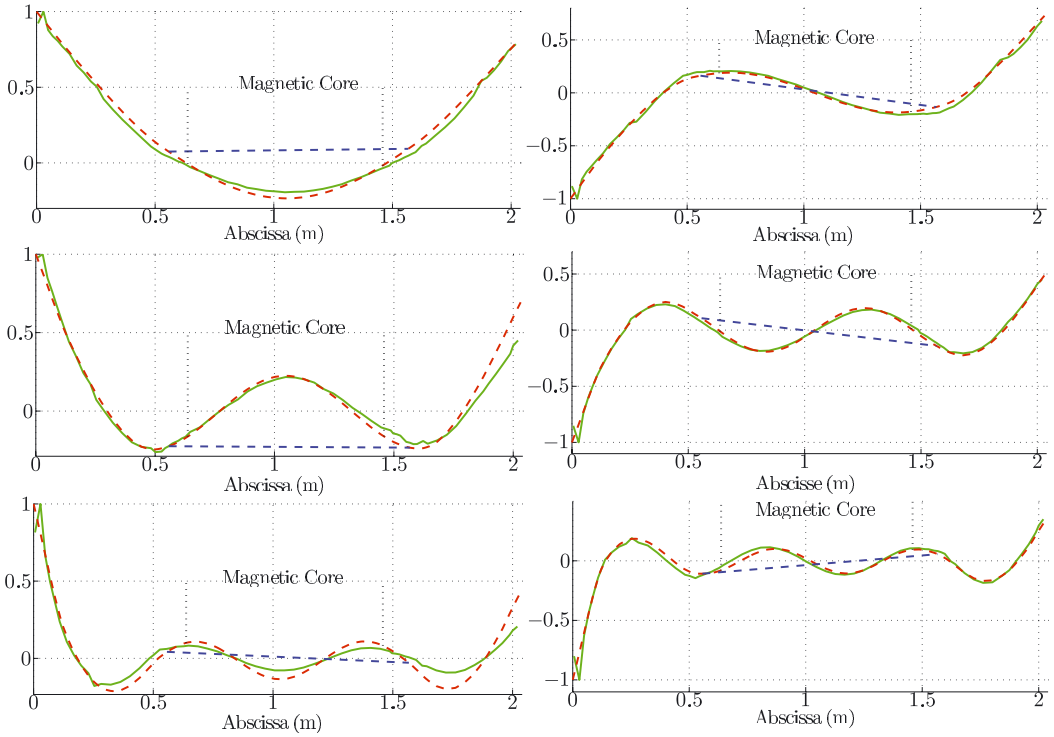

Fig. 16. View of the first six predicted mode shapes (−− (rotor), −− (tie rods)) and measured mode shapes (−).

The correct correlation between the predicted and measured mode shapes, illustrated in Figure 16, is quantified by the correlation matrix NCO and determined by the following relation:

$$\mathrm{NCO}\left(\hat{\varphi}_i, \tilde{\varphi}_j\right) = \frac{\left(\hat{\varphi}_i^t \tilde{M} \tilde{\varphi}_j\right)^2}{\left(\hat{\varphi}_i^t \tilde{M} \hat{\varphi}_i\right) \cdot \left(\tilde{\varphi}_j^t \tilde{M} \tilde{\varphi}_j\right)}, \quad i, j = 1, \ldots, m \tag{45}$$

with $\hat{\varphi}_i$ the ith measured mode shape, $\tilde{\varphi}_j$ the jth mode shape of the condensed model, $\tilde{M}$ the condensed mass matrix and m the number of modes considered. Colinearity and above all orthogonality are then estimated and verified, something that is not guaranteed by the MAC matrix [31]. The advantage of the NCO matrix, Equation (45) is that it highlights the notion of orthogonality introduced by the modal method theory that stipulates that the orthogonality between two mode shapes is always defined with respect to the mass (and stiffness) matrix. Figure 17 is a representation of the NCO matrix; the diagonal terms, higher than 0.9, and the extra-diagonal terms, lower than 0.1, corroborate the satisfactory correlation between the two sets of measured $\hat{\varphi}$ and predicted $\tilde{\varphi}$ mode shapes.

6 Conclusion

The identification procedure was performed on an industrial structure and permitted establishing a finite-element model of beams containing few d.o.f., providing an advantage when predicting the dynamic of rotors with complex designs. The tie rods were modeled independently of the magnetic mass while considering the axial load applied on them. The combination of an energy based functional with the Guyan reduction is an efficient solution for identifying the parameters of a finite element model by using a priori non compatible data, i.e. natural frequencies and mode shapes. The constitutive properties of the laminated core of a squirrel cage rotor were identified correctly in so far as the number of modes used was sufficiently representative of the dynamic of the structure tested. This article described the first step of an approach to modeling the lateral dynamic behavior of squirrel cage rotors, by presenting the results obtained on the structure at rest. The next challenge will be to take into account the centrifugal effects applied to the tie rods that exert an additional axial load by rigidifying the laminated core while the system is in rotation.

Acknowledgements. The authors would like to thank Converteam for its technical assistance and its authorization to publish this research.

Appendix A: Elementary stiffness matrices

$$ {}^eK_f = \frac{{}^eE\,{}^eI_{G_y}}{(1+{}^e\phi_y)\,{}^el^3} \times \begin{bmatrix} 12 & -6{}^el & -12 & -6{}^el \\ & (4+{}^e\phi_y)\,{}^el^2 & 6{}^el & (2-{}^e\phi_y)\,{}^el^2 \\ & & 12 & 6{}^el \\ \text{Sym.} & & & (4+{}^e\phi_y)\,{}^el^2 \end{bmatrix} \tag{A.1}$$

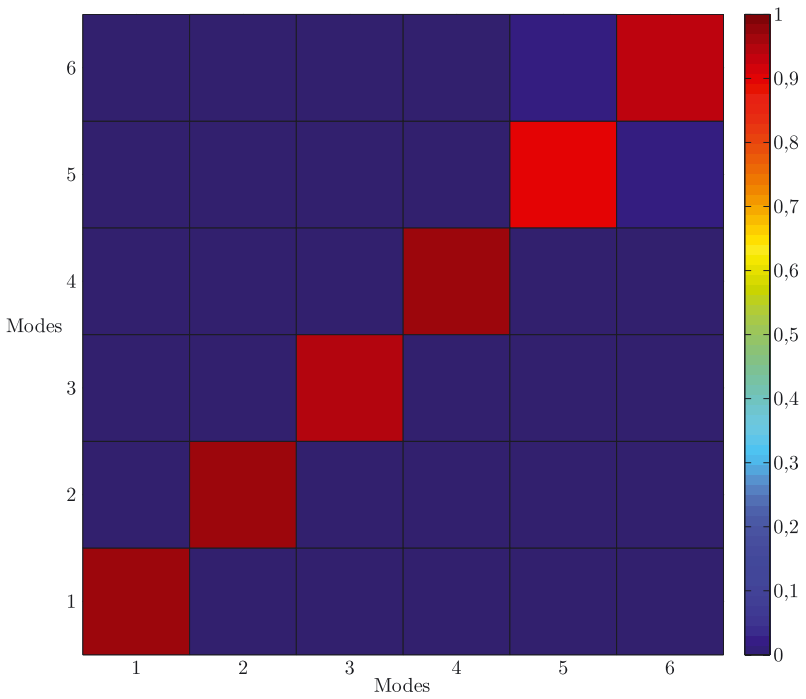

Fig. 17. View of the NCO correlation matrix (Normalized Cross Orthogonality).

with ${}^e\phi_y$ being the elementary shear factor defined as follows:

$$ {}^e\phi_y = \frac{12\,{}^eE\,{}^eI_{G_y}}{{}^eG\,{}^ek\,{}^eS\,{}^el^2} \tag{A.2} $$

where ${}^eE$ is the elementary Young's modulus, ${}^eI_{G_y}$ the second moment of inertia of the elementary cross section, ${}^eG$ the elementary shear modulus, ${}^eS$ the elementary cross section, ${}^el$ the elementary length and ${}^ek$ the shear coefficient of the elementary cross section defined by the expression:

$$ {}^ek = \frac{6\left(1+{}^e\upsilon\right)\left(1+a^2\right)^2}{\left(7+6{}^e\upsilon\right)\left(1+a^2\right)^2+\left(20+12{}^e\upsilon\right)a^2} $$

$$ \text{with} \quad {}^ea = \frac{{}^ed^{\text{int}}}{{}^ed^{\text{ext}}} \tag{A.3} $$

where ${}^ed^{\text{int}}$ and ${}^ed^{\text{ext}}$ are respectively the inner and outer diameters of an elementary cross section ${}^eS$ and ${}^e\upsilon$ is the elementary Poisson ratio.

$$ {}^eK_G = \frac{{}^eF_N}{60\left(1+{}^e\phi_y\right)^2{}^el} \times \begin{bmatrix} k_{G_{11}} & -6{}^el & -k_{G_{11}} & -6{}^el \\ & k_{G_{22}} & 6{}^el & -k_{G_{24}} \\ & & k_{G_{11}} & 6{}^el \\ \text{Sym.} & & & k_{G_{22}} \end{bmatrix} \tag{A.4} $$

with

$$ \begin{aligned} k_{G_{11}} &= 36+60{}^e\phi_y+30{}^e\phi_y^2 \\ k_{G_{22}} &= \left(8+10{}^e\phi_y+5{}^e\phi_y^2\right){}^el^2 \\ k_{G_{24}} &= \left(2+10{}^e\phi_y+5{}^e\phi_y^2\right){}^el^2 \end{aligned} $$

where ${}^eF_N$ is an elementary axial force and ${}^e\phi_y$ is defined in Equation (A.2).

Appendix B: Elementary mass matrices

$$ {}^eM_v = \frac{{}^e\rho\,{}^eS\,{}^el}{840\left(1+{}^e\phi_y\right)^2} \times \begin{bmatrix} m_{v_{11}} & m_{v_{12}} & m_{v_{13}} & m_{v_{14}} \\ & m_{v_{22}} & -m_{v_{14}} & m_{v_{24}} \\ & & m_{v_{11}} & -m_{v_{12}} \\ \text{Sym.} & & & m_{v_{22}} \end{bmatrix} \tag{B.1} $$

with

$$ \begin{aligned} m_{v_{11}} &= \left(312+588{}^e\phi_y+280{}^e\phi_y^2\right) \\ m_{v_{12}} &= -\left(44+77{}^e\phi_y+35{}^e\phi_y^2\right){}^el \\ m_{v_{13}} &= \left(108+252{}^e\phi_y+140{}^e\phi_y^2\right) \\ m_{v_{14}} &= \left(26+63{}^e\phi_y+35{}^e\phi_y^2\right){}^el \\ m_{v_{22}} &= \left(8+14{}^e\phi_y+7{}^e\phi_y^2\right){}^el^2 \\ m_{v_{24}} &= -\left(6+14{}^e\phi_y+7{}^e\phi_y^2\right){}^el^2 \end{aligned} $$

where ${}^e\rho$ is the elementary density.

$$ {}^eM_\theta = \frac{{}^e\rho\,{}^eI_{G_y}\,{}^el}{840\left(1+{}^e\phi_y\right)^2} \times \begin{bmatrix} m_{\theta_{11}} & m_{\theta_{12}} & -m_{\theta_{11}} & m_{\theta_{12}} \\ & m_{\theta_{22}} & -m_{\theta_{12}} & m_{\theta_{24}} \\ & & m_{\theta_{11}} & -m_{\theta_{12}} \\ \text{Sym.} & & & m_{\theta_{22}} \end{bmatrix} \tag{B.2} $$

with

$$ \begin{aligned} m_{\theta_{11}} &= 1008/{}^el^2 \\ m_{\theta_{12}} &= -\left(84-420{}^e\phi_y\right)/{}^el \\ m_{\theta_{22}} &= \left(112+140{}^e\phi_y+280{}^e\phi_y^2\right) \\ m_{\theta_{24}} &= -\left(28+140{}^e\phi_y-140{}^e\phi_y^2\right) \end{aligned} $$

References

[1] G. Mogenier, R. Dufour, G. Ferraris-Besso, L. Durantay, N. Barras, Identification of lamination stack properties. application to high speed induction motors, IEEE Trans. Ind. Electron. 57 (2010) 281–287

[2] R. Belmans, W. Heylen, A. Vandenput, W. Geysen, Influence of rotor-bar stiffness on the critical speed of an induction motor with an aluminium squirrel cage, in: IEEE Proc. B: Electric power Applications, Vol. 131, 1984, pp. 203–208

[3] J. McClurg, Advantages of stiff shaft design on high speed, high horsepower squirrel cage induction motors and generators, in: 34th record of Conference Papers, Annual Petroleum and Chemical Industry Conference, 1987, pp. 259–263

[4] S. Chang, D. Lee, Robust design of a composite air spindle, Polym. Compos. 23 (2002) 361–371

[5] J. Ede, D. Howe, Z. Zhu, Rotor resonances of high-speed permanent-magnet brushless machines, IEEE Trans. Ind. Appl. 38 (2002) 1542–1548

[6] S. Garvey, J. Penny, M. Friswell, A. Lees, The stiffening effect of laminated rotor cores on flexible-rotor electrical machines, IMechE Event Publications 2004 (2004) 193–202

[7] Y.S. Chen, Y.D. Cheng, J.J. Liao, C.C. Chiou, Development of a finite element solution module for the analysis of the dynamic behavior and balancing effects of an induction motor system, Finite Elem. Anal. Des. 44 (2008) 483–492

[8] S. Garvey, The vibrational behaviour of laminated components in electrical machines, in: The 4th International Conference on Electrical Machines and Drives, 1989, pp. 226–231

[9] S. Long, Z. Zhu, D. Howe, Vibration behaviour of stators of switched reluctance motors, IEEE Proc.: Electric Power Applications, 148 (2001) 257–264

[10] Z. Tang, P. Pillay, A.M. Omekanda, C. Li, C. Cetinkaya, Effects of material properties on switched reluctance motor vibration determination, in: Conference Record – IAS Annual Meeting (IEEE Industry Applications Society), Vol. 1, 2003 IEEE Industry Applications Conference, 38th IAS Annual Meeting – Crossroads To Innovation, Institute of Electrical and Electronics Engineers Inc., 2003, pp. 235–241

[11] Y.-C. Kim, K. K-W, Influence of lamination pressure upon the stiffness of laminated rotor, JSME Int. J. Ser. C Mech. Syst., Machine Elements and Manufacturing 49 (2006) 426–431

[12] C. Lee, T. Kam, Identification of mechanical properties of elastically restrained laminated composite plates using vibration data, J. Sound Vib. 295 (2006) 999–1016

[13] X. Feng, J. Zhou, Y. Fan, Method for identifying subregional material parameters of concrete dams using modal data, Acta Mech. Sol. Sin. 16 (2003) 88–94

[14] J. Cugnoni, T. Gmür, A. Schorderet, Inverse method based on modal analysis for characterizing the constitutive properties of thick composite plates, Comput. Struct. 85 (2007) 1310–1320

[15] T. Lauwagie, K. Lambrinou, S. Patsias, W. Heylen, J. Vleugels, Resonant-based identification of the elastic properties of layered materials: application to air-plasma sprayed thermal barrier coatings, NDT and E Int. 41 (2008) 88–97

[16] I. Ojalvo, Efficient computation of mode-shape derivatives for large dynamic systems, AIAA J. 25 (1987) 1386–1390

[17] Y. Min, L. Zhong-Sheng, W. Da-Jun, Comparison of several approximate modal methods for computing mode shape derivatives, Comput. Struct. 62 (1997) 381–393

[18] R. Nelson, Simplified calculation of eigenvector derivatives, AIAA J. 14 (1976) 1201–1205

[19] S. Andrieux, T. Baranger, Energy methods for Cauchy problems of evolutions equations, J. Phys.: Conf. S. 135 (2008)

[20] R.J. Guyan, Reduction of stiffness and mass matrices, AIAA J. 3 (1965) 380–380

[21] L.F.F. Miguel, R.C.R. de Menezes, L.F.F. Miguel, Mode shape expansion from data-based system identification procedures, Mec. Compu., Dynam. Vibr. (A) 25 (2006) 1593–1602

[22] F. Kuratani, T. Shimada, T. Yamano, T. Ogawa, Structural modification with mode shape expansion for rib stiffeners, JSME Int. J. S. C Mech. Syst., Machine Elements and Manufacturing 49 (2006) 771–778

[23] J.-S. Przemieniecki, Theory of Matrix Structural Analysis, 46th edition, Dover Publications, INC., New York, 1985

[24] M. Lalanne, G. Ferraris, Rotordynamics Prediction in Engineering, 2nd edition, John Wiley and Sons Ltd, New York, 1998

[25] G. Genta, Dynamics of Rotating Systems, Springer Verlag, 2005

[26] G. Cowper, The shear coefficient in Timoshenko's beam theory, J. Appl. Mech. 33 (1966) 335–340

[27] T. Gmür, Dynamique des structures: Analyse modale numérique, Presses Polytechniques et Universitaires Romandes, 1997

[28] H. Nielsen, Damping parameter in Marquardt's method, Technical report, Technical Univ. of Denmark, 1999

[29] D. Marquardt, An algorithm for least-squares estimation of nonlinear parameters, J. Soc. Ind. Appl. Math. 11 (1963) 431–441

[30] G. Mogenier, R. Dufour, G. Ferraris-Besso, L. Durantay, N. Barras, Optimization procedure for identifying constitutive properties of high speed induction motor, Proc. 2008 Int. Conf. Electrical Machines, ICEM'08, 2008

[31] C. Morales, Comments on the MAC and the NCO, and a linear modal correlation coefficient, J. Sound Vib. 282 (2005) 529–537